Journal of *Marine Science and Engineering*

MDPI

Article

A Methodology for Susceptibility Assessment of Wave-Induced Seabed Liquefaction in Silt-Dominated Nearshore Environments

Yueying Wang [1], Xingsen Guo [1,2,*], Jinkun Liu [3], Fang Hou [3], Hong Zhang [4], Han Gao [1] and Xiaolei Liu [1,5,*]

[1] Shandong Provincial Key Laboratory of Marine Environment and Geological Engineering, Ocean University of China, Qingdao 266100, China; wyy98@stu.ouc.edu.cn (Y.W.); gaohan9009@stu.ouc.edu.cn (H.G.)
[2] Department of Civil, Environmental, and Geomatic Engineering, University College London, London WC1E 6BT, UK
[3] Sinopec Petroleum Engineering Corporation, Dongying 257026, China; speljk@163.com (J.L.); slecchf@126.com (F.H.)
[4] College of Engineering, Ocean University of China, Qingdao 266100, China; zhanghong9645@ouc.edu.cn
[5] Laboratory for Marine Geology, Qingdao Marine Science and Technology Center, Qingdao 266237, China
* Correspondence: xingsen.guo@ucl.ac.uk (X.G.); xiaolei@ouc.edu.cn (X.L.)

Abstract: Wave-induced seabed liquefaction significantly jeopardizes the stability of marine structures and the safety of human life. Susceptibility assessment is key to enabling spatial predictions and establishing a solid foundation for effective risk analysis and management. However, the current research encounters various challenges, involving an incomplete evaluation system, poor applicability of methods, and insufficient databases. These issues collectively hinder the accuracy of susceptibility assessments, undermining their utility in engineering projects. To address these challenges, a susceptibility assessment method with the safety factor was developed as the key assessment parameter, allowing for a comprehensive susceptibility assessment across the silt-dominated nearshore environment using Empirical Bayesian Kriging (EBK). The safety factor is determined by combining the cyclic stress ratio (CSR) and the cyclic resistance ratio (CRR), which characterize wave loadings and sediment properties in the study area, respectively. This method was applied in the Chengdao region of the Yellow River Estuary, China, a typical silt-dominated nearshore environment where wave-induced liquefaction events have been reported as being responsible for multiple oil platform and pipeline accidents. By collecting the regional wave and seabed sediment data from cores spanning from 1998 to 2017, the safety factors were calculated, and a zonal map depicting the susceptibility assessment of wave-induced seabed liquefaction was created. This study can serve as a valuable reference for the construction and maintenance of marine engineering in liquefaction-prone areas.

Keywords: wave-induced seabed liquefaction; susceptibility assessment; safety factor; cyclic stress ratio; cyclic resistance ratio; Empirical Bayesian Kriging

Citation: Wang, Y.; Guo, X.; Liu, J.; Hou, F.; Zhang, H.; Gao, H.; Liu, X. A Methodology for Susceptibility Assessment of Wave-Induced Seabed Liquefaction in Silt-Dominated Nearshore Environments. *J. Mar. Sci. Eng.* **2024**, *12*, 785. https://doi.org/10.3390/jmse12050785

Academic Editor: Jianhong Ye

Received: 9 April 2024
Revised: 24 April 2024
Accepted: 27 April 2024
Published: 8 May 2024

1. Introduction

Seabed liquefaction is a phenomenon associated with sediment instability. Under the influence of external forces (e.g., wave action, earthquakes, and human activities), the internal stress state of the sediment changes. Specifically, when the excess pore pressure is equivalent to the effective stress of the overlying sediment, the state of the sediment changes from solid to fluid, and the sediment becomes liquefied [1–3]. Wave-induced seabed liquefaction is caused by an external load cyclically applied to the seabed, generating differential loading on the seafloor through pressure waves that induce a series of cyclic shear stresses in the underlying sediment. If the induced shear stress exceeds the strength, it may lead to substantial deformation or liquefaction failure [1]. This sequence of this event can lead to various engineering safety problems and compromise the stability of

marine structures [4,5]. It poses significant risks to human lives and property, as illustrated in Figure 1.

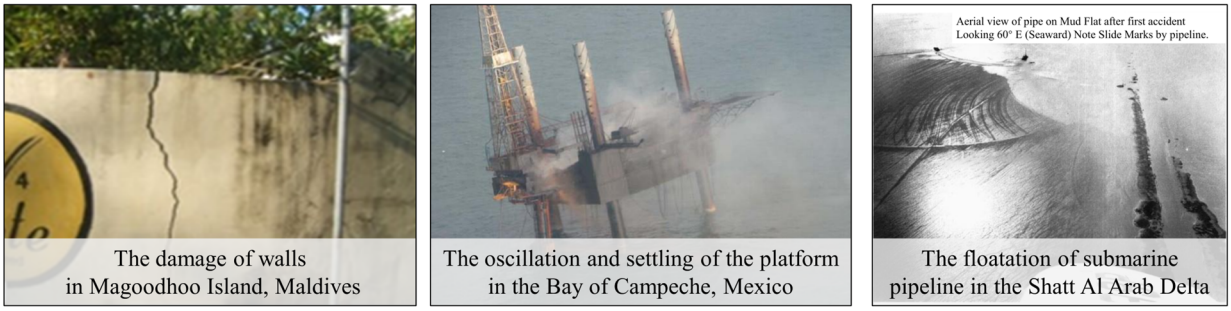

Figure 1. Effects of seabed liquefaction on coastal environments. Because of seabed liquefaction, differential settlement of coastal areas causes cracks in nearshore houses and walls (**a**); sediment strength is reduced, causing destabilization of offshore platforms (**b**); and the seabed soil around the trench turned into a dense liquid that flooded the trench and caused the pipeline to fail (**c**) (images from Di Fiore et al. [6], Chávez et al. [7], and Damgaard et al. [8]).

To predict and evaluate the occurrence probability and severity of seabed liquefaction effectively, numerous researchers have started applying risk assessment and management techniques to this field [9–12]. These studies contribute to the quantitative analysis of the spatial extent of disasters, geological disaster mechanisms, and triggering factors [13,14]. The insights derived from these analyses provide recommendations for pre-disaster planning, disaster response, and post-disaster recovery efforts, ultimately mitigating losses. This field has garnered significant attention from governments, industries, and the scientific research community [15]. Nevertheless, the complex nature of wave-induced seabed liquefaction mechanisms makes it challenging to identify assessment factors. This difficulty hinders the advancement of risk assessment and management in this specific context. Among these challenges, the susceptibility assessment of seabed liquefaction emerges as a pivotal aspect in the risk assessment of seabed liquefaction. It directly impacts the accuracy of risk assessment and requires the advancement of reliable theories and practical methodologies. Susceptibility assessment of wave-induced seabed liquefaction primarily involves the creation of a disaster inventory, selection of conditioning factors, and identification of assessment methods [16]. Because of the complexity of wave-induced seabed liquefaction mechanisms, the choice of different monitoring tools for liquefaction under different sediment conditions directly affects the establishment of the disaster inventory and the selection of condition factors, and ultimately determines the research methods [17]. Therefore, priority should be given to addressing the accuracy of susceptibility assessment methods. The existing research methods lack the capability to adequately evaluate susceptibility across various sediment types, highlighting the necessity for the development of new methods to enhance evaluation accuracy [17,18].

Currently, susceptibility assessment methods for seabed liquefaction predominantly revolve around statistical approaches and deterministic analysis. The statistical approach enables both qualitative and quantitative evaluations of geological disasters by employing statistical principles to describe relationships among conditioning factors [19]. Consequently, this method, including bivariate statistical analysis, multivariate statistical analysis, and machine learning (such as neural network models and maximum entropy models), finds extensive application in the susceptibility analysis of marine geological disasters [16]. However, the statistical approach primarily focuses on the probability of disasters and allocates less consideration to the mechanism of disasters [19]. In contrast, the deterministic approach focuses on the mechanics of disaster occurrence. It has gained significant attention from researchers for its ability to quantitatively assess susceptibility to wave-induced seabed liquefaction [16]. A 3-D assessment methodology for seabed liquefaction has been

proposed, based on cyclic triaxial tests, liquefaction potential evaluation criteria, and the nearshore spectral windwave (NSW) model. Nonetheless, this method did not take into account the effects of pore water pressure dissipation that could take place during a storm period, rendering it unsuitable for completing the susceptibility assessment of shallow sediment liquefaction [20]. Di Fiore et al. explored wave-induced seabed liquefaction through cyclic triaxial tests and evaluated the liquefaction potential of the Magoodhoo coralline island and coastal regions [6]. However, their calculation method for CSR (the cyclic stress ratio) was only applicable to wave heights ranging from 0.2 to 3.0 m. Furthermore, the evaluation factor was solely wave height, resulting in an oversimplified assessment model that compromises result accuracy [6]. In summary, the current evaluation method lacks a comprehensive consideration of evaluation factors for generating zoning maps based on evaluation results, and it falls short in assessing different sediment types. Therefore, it is crucial to introduce a more precise methodology to overcome these challenges.

In this study, a method for the susceptibility assessment of wave-induced seabed liquefaction is introduced, with a particular focus on safety factors, which have been widely used in susceptibility assessment for various natural processes. This method characterizes wave loading through CSR and employs CRR (the cyclic resistance ratio) to represent sediment properties to calculate safety factors. The calculation of CSR follows the method proposed by Ishihara et al. [21], while CRR analysis integrates considerations of sediment characteristics. Utilizing this approach in the Chengdao region involved calculating CSR values for diverse wave recurrence periods (5-year, 10-year, and 25-year). Concurrently, sediment properties determined CRR at varying depths, assessed through cyclic triaxial torsion shear tests at sampling points. Establishing the smallest safety factor among these points facilitated the identification of the wave-induced seabed liquefaction susceptibility assessment. The susceptibility zoning map was generated using Empirical Bayesian Kriging (EBK) in the Arc Geographic Information System 10.7 (ArcGIS 10.7). This method is applicable to seabed areas with silt-dominated environments and can maximize the accuracy of small-scale susceptibility assessments of wave-induced seabed liquefaction, even when data are limited.

2. Methodology

2.1. Susceptibility Assessment Model of Wave-Induced Seabed Liquefaction

Currently, various methods exist for the susceptibility assessment of wave-induced seabed liquefaction, commonly categorized as a statistical approach or deterministic analysis [16]. Deterministic analysis, as discussed earlier, allows for a more comprehensive exploration of the mechanism behind wave-induced seabed liquefaction, aligning closely with its characteristics and thus finding extensive application [16]. The safety factor employed in this study falls within a deterministic analysis, offering quantitative insights into liquefaction susceptibility. This method was initially proposed by Seed et al. in 1971 [22]. Its versatility allows for application across study areas with diverse sediment types and various scenarios, promising a more precise susceptibility of wave-induced seabed liquefaction [23]. This method employs CSR to signify the extent of external load impact on sediment liquefaction and uses CRR to indicate sediment resistance properties [22,24]. The safety factor can be determined by comparing CSR and CRR at varying depths according to Equation (1):

$$FS = \frac{CRR}{CSR} \quad (1)$$

where FS is the safety factor; CSR is the cyclic stress ratio; and CRR is the cyclic resistance ratio. The seabed liquefaction susceptibility of each area is further classified according to the characteristics of the study area and the probability of liquefaction, combined with the safety factor [25].

It is usually considered that the liquefaction will not occur in the region when $FS > 1$ and that the liquefaction will occur in the region when $FS < 1$. The interrelation between the safety factor and reliability had been explored, proposing that the safety factor can be

specified based on reliability levels, and the allocation of the safety factor should be based on having the same reliability associated with each failure mode [26]. The influence of geotechnical parameter variability on the liquefaction potential of tailing dams has been explored [27]. The safety factor for different liquefaction probabilities has been compared, highlighting the use of probabilistic methods for failure probability and the safety factor against liquefaction analysis [27]. Therefore, the division intervals of safety factors need to be determined based on the actual conditions of the research area, considering the characteristics of disaster events, and based on different liquefaction probabilities.

2.2. Cyclic Stress Ratio

CSR represents the ratio of the amplitude of shear stress to the effective confining stress, which is used to quantify the deformability or strength of soils under cyclic loading conditions [22]. According to linear wave theory, a wave event can be described by fundamental wave characteristics [28]. Thus, various authors have suggested simplifying the CSR calculation based on this theory [21]. When analyzing wave conditions, the following criteria must be considered: (1) to reduce computational complexity, the irregular loads, induced by actual waves on the seabed surface, are simplified to uniform loads and (2) because this method is designed for shallow sea areas, it assumes that all waves are linear [23,29,30].

Regarding the characteristics of waves, they can be considered to consist of an infinite number of wave trains with the same amplitude and wavelength. The passage of such an array of waves over the ocean creates harmonic pressure waves on the seafloor, increasing the pressure under the crest and reducing it under the trough, as shown in Figure 2 [21]. Considering the rectangular coordinate system, the sea surface elevation of a wave field η may be represented by Ishihara and Yamazaki's Equation (2) [21]:

$$\eta(x,t) = \frac{H}{2}\cos(kx - \omega t) \tag{2}$$

where H is the wave height, $k = \left(\frac{2\pi}{L}\right)$ is the wave number, L is the wave length, $\omega = \left(\frac{2\pi}{T}\right)$ is the wave frequence, T is the wave period, x is the spatial coordinate in the x direction, and t is the time coordinate. For linear waves, k and ω are related by the dispersion relationship according to Equation (3) [1]:

$$\omega^2 = gk\tanh kd \tag{3}$$

where g is the gravitational acceleration. Equation (3) also can be rewritten as Equation (4):

$$L = \frac{gT^2}{2\pi}\tan h\left(\frac{2\pi d}{L}\right) \tag{4}$$

where L is the wave length, T is the wave period, and d is the water depth.

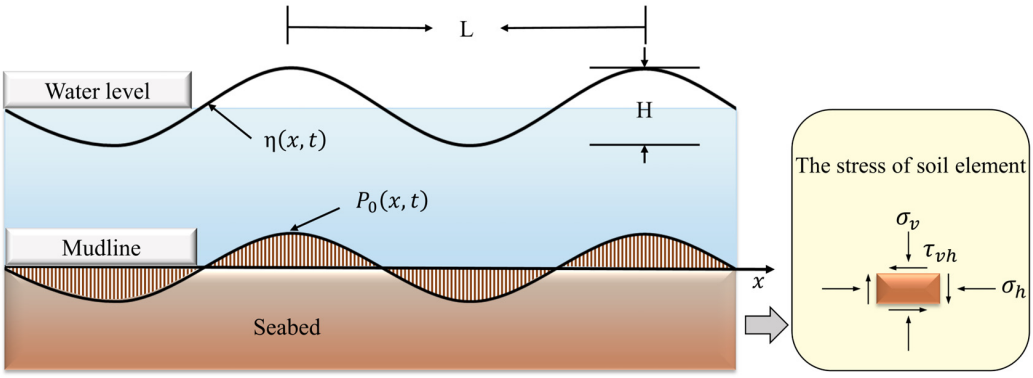

Figure 2. Wave-induced cyclic pressures and stresses.

Regarding the characteristics of wave-induced cyclic stress, the seabed deposit is assumed to consist of a homogeneous elastic material extending to an infinite depth. Boussinesq's classical solution for the two-dimensional plane strain problem can be employed to calculate the stresses acting on it [31]. The stress induced in the seabed is, therefore, analyzed by applying a sinusoidally changing load on the horizontal surface from minus to plus infinity according to Equation (5):

$$p(x) = p_0 \cos\left(\frac{2\pi}{L}x - \frac{2\pi}{T}t\right) \tag{5}$$

where L is the wave length, x is the spatial coordinate in the x direction, T is the wave period, and t is the time coordinate. According to the small amplitude wave, the amplitude of the pressure fluctuation exerted on the sea bottom, p_0, by the travelling wave is given by Horikawa's Equation (6) [32]:

$$p_0 = \frac{\rho_w g H}{2\cos\mathrm{h}(2\pi d/L)} \tag{6}$$

where ρ_w is the density of seawater, g is the gravitational acceleration, H is the wave height, d is the water depth, and L is the wave length. Considering the uniform distribution and infinite depth of the sediments, the amplitude of maximum shear stress can be determined by analyzing the relationship between the horizontal stress, vertical stress, and shear stress of the harmonic pressure wave. The analysis utilizes the classical Boussinesq solution for two-dimensional plane strain problems according to Equation (7) [21]:

$$\tau_{vh} = 2\pi z p_0 \frac{1}{L}\left(e^{-2\pi z/L}\right) \tag{7}$$

where τ_{vh} is the shear stress, p_0 is the amplitude of the pressure fluctuation exerted on the sea bottom, L is the wave length, and z is the sampling depth. Since the magnitude of σ_v' is expressed by $\sigma_v' = \rho' g z$, CSR is given by Equation (8) [21]:

$$\mathrm{CSR} = \frac{(\tau_{vh})_{max}}{\sigma_v'} = \frac{2\pi p_0}{\rho' g L}\exp\left(-\frac{2\pi z}{L}\right) \tag{8}$$

where τ_{vh} is the shear stress, σ_v' is the vertical effective stress, p_0 is the amplitude of the pressure fluctuation exerted on the sea bottom, ρ' is the submerged unit mass of soils in the seabed, g is the gravitational acceleration, L is the wave length, and z is the sampling depth. According to the formula, comprehensive data on fundamental wave characteristics like wave height, wavelength, wave period, and water depth is essential. This information not only allows for the calculation of CSR but also facilitates the simulation of CSR under extreme wave conditions.

2.3. Cyclic Resistance Ratio

CRR is a parameter that measures the resistance of sediments to liquefaction. It represents the ratio between the average cyclic shear stress and the vertical effective stress of sediments [22]. Different sediment types require specific calculation methods, and the operational ease varies among various test methods. The field test methods of CRR under seismic liquefaction were summarized by referring to the research results of Youd et al., as shown in Table 1 [24]. The primary field test includes SPT (Standard Penetration Test), CPT (Cone Penetration Test), measurement of V_S (Shear Wave Velocity), and BPT. SPT is a test conducted during a test boring in the field to measure the approximate soil resistance to penetration of a split-spoon sampler at various depths below the ground surface [33]. This test was intended to measure the number of blows required to drive a standard sampling tube into the ground to a certain depth [34]. As for CPT, an elongated metal probe (typically conical in shape) is pushed into the ground, and the resistance and soil displacement during the penetration process are measured. It is performed by pushing an instrumented probe with a specific diameter into the earth at a constant speed while

simultaneously measuring the cone resistance and sleeve friction resistance [35]. The V_S test is a geoengineering test used to determine the shear wave velocity in soil or rock. A shear wave is a wave that propagates through shear deformation in a material, and its speed is related to the shear modulus of the material. Shear wave velocity tests are often used to study the elastic properties and mechanical behavior of soil or rock [36]. When conducting liquefaction assessments, SASWs are useful for V_S profile surveys of liquefaction sites [37]. Becker penetration resistance is defined as the number of blows required to drive the casing through an increment of 300 mm [24]. The formula for calculating CRR corresponding to the above method is mentioned in Table 2. It is essential to choose the appropriate method based on the actual conditions of CRR calculation, significantly enhancing the accuracy of CRR and FS and consequently improving the precision of susceptibility assessment results.

Table 1. Comparison of advantages and disadvantages of various field tests for CRR.

Feature	Test Type			
	SPT [38]	**CPT [39]**	**V_S [37]**	**BPT [24]**
Types of stress–strain behavior influencing test	Partially drained, large strain	Drained, large strain	Small strain	Partially drained, large strain
Quality control and repeatability	Poor to good	Very good	Good	Poor
Soil types in which the test is recommended	No gravel	No gravel	All	Gravel

Table 2. Summary of methods for calculating CRR.

Source	Formula	Testing Method
[38]	$\mathrm{CRR} = \exp\left[\frac{(N_{1,60}*(1+\theta_1*\mathrm{FC})-\theta_6*\ln(M_w)-\theta_3*\ln\left(\frac{\sigma'_v}{P_a}\right)+\theta_4*\mathrm{FC}+\sigma_\varepsilon*\Phi^{-1}(P_L)}{\theta_6}\right]$	SPT
[39]	$\mathrm{CRR} = \exp\left\{\frac{\left[q_{c,1}^{1.045}+q_{c,1}\left(0.110*R_f\right)+\left(0.001*R_f\right)-0.848*\ln(M_w)-0.002*\ln(\sigma'_v)-20.923+1.632*\Phi^{-1}(P_L)\right]}{7.177}\right\}$	CPT
[37]	$\mathrm{CRR} = \exp\left\{\frac{\left[(0.0073*V_{s1})^{2.8011}-2.6168*\ln(M_w)-0.0099*\ln(\sigma'_v)+0.0028*\mathrm{FC}+0.4809*\Phi^{-1}(P_L)\right]}{1.946}\right\}$	SASW

Note: $N_{1,60}$ is the standard penetration test blowcount value corrected for overburden, energy, equipment, and procedural factors; θ_i is the set of unknown model coefficients; FC is the fines content; M_w is the earthquake moment magnitude; σ'_v is the vertical effective stress; P_a is the atmospheric pressure (1 atm); Φ is the standard cumulative normal distribution; P_L is the probability of triggering of liquefaction; $q_{c,1}$ is the normalized cone tip resistance; R_f is the friction ratio; V_{s1} is the effective stress normalized shear-wave velocity.

The above method is suitable for the calculation of CRR in the terrestrial environment. However, the monitoring difficulty in the marine environment is greater than that in the terrestrial environment, and the in situ test is more difficult and costly [40,41]. Therefore, the laboratory test has attracted more attention in the field of submarine geological disaster susceptibility assessment. The cyclic triaxial torsion shear test is a widely used sediment testing method suitable for saturated sand and saturated silt in nearshore areas [31]. It offers a streamlined computation process with fewer evaluation factors, facilitating a rapid assessment of sediment resistance to liquefaction. This test reflects the cyclic loading characteristics of the sediment, a characteristic that is one of the determining factors in the susceptibility assessment of wave-induced seabed liquefaction [31]. Introduced by Ishihara et al., this method selects the dynamic stress ratio when the double amplitude deviator strain reaches 5% as CRR for the sediments at the given point [21]. Based on this standard, they conducted a large number of cyclic triaxial tests, summarized the relevant rules, and proposed the calculation according to the relative density of sediments and the coefficient of earth pressure at rest, as shown in Equation (9) [21]:

$$\mathrm{CRR} = 0.0019 * D_r * \frac{1 + 2K_0}{3} \tag{9}$$

where D_r is the relative density and K_0 is the coefficient of earth pressure at rest. However, this method is applicable to sandy sediments, but not to silt, so some scholars have found another universal rule, which indicates that the cyclic stress ratio at 100 load cycles is determined to be closest to this criterion, as illustrated in Equation (10) [21,23]. Since there exists an exponential relationship between the number of cyclic loadings and the cyclic dynamic stress in the cyclic triaxial test, as depicted in Equation (11), the CRR can be calculated by fitting this exponential relationship with convincing data obtained through the tests [23].

$$\mathrm{CRR} = \left(\frac{\tau_L}{\sigma_v'}\right)_{100} = \left(\frac{\sigma_d}{2\sigma_C}\right)_{100} = \frac{3\sigma_d}{2(\sigma_1 + \sigma_3)} \tag{10}$$

where τ_L is the horizontal shear stress, σ_v' is the vertical effective stress, σ_d is the cyclic dynamic stress, σ_C is the average consolidation pressures, σ_1 is the axial consolidation pressures, and σ_3 is the lateral consolidation pressures.

$$\frac{\tau_L}{\sigma_v'} = \mathrm{a} * \ln N + \mathrm{b} \tag{11}$$

where τ_L is the horizontal shear stress, σ_v' is the vertical effective stress, N is the number of cyclic loadings, and a and b are the fitting coefficients.

2.4. Geospatial Interpolation

The previous process allows us to calculate the safety factor for a specific location. However, to complete a susceptibility assessment of marine geological disasters for the entire study area, spatial interpolation tools within the Arc Geographic Information System 10.7 (ArcGIS 10.7) need to be employed. These tools maximize the utilization of existing data points to comprehensively delineate the susceptibility assessment of liquefaction across the entire area [9]. To reconstruct a continuous attribute distribution over the entire study area, the spatial interpolation method utilizes a finite set of sampling points $S = \{(x_i, f_i),\ i = 1, 2, 3, \ldots, n\}$ to establish an interpolation function $(f : x \to x)$ that estimates attribute values at any given data point within the study area [10]. Spatial interpolation can be categorized into geostatistical interpolation and deterministic interpolation. A widely used geostatistical interpolation method is EBK, which is valued for its simplicity and accurate results [42,43]. This method accounts for introduced error by estimating the underlying semivariance function, whereas other kriging methods calculate the semivariance function from a known data location and apply this single semivariance function to make predictions at an unknown location [9,44]. By not considering the uncertainty in the estimation of the semivariance function, other kriging methods underestimate the standard error of the prediction, while the EBK is more accurate [44]. Additionally, EBK requires minimal interactive modeling, excels at predicting unstable data, and is particularly well-suited for smaller datasets [9].

2.5. Susceptibility Assessment System of Wave-Induced Seabed Liquefaction

Based on the above discussion of the susceptibility assessment and spatial interpolation methods, the specific steps for partitioning the susceptibility assessment of wave-induced seabed liquefaction are shown in Figure 3.

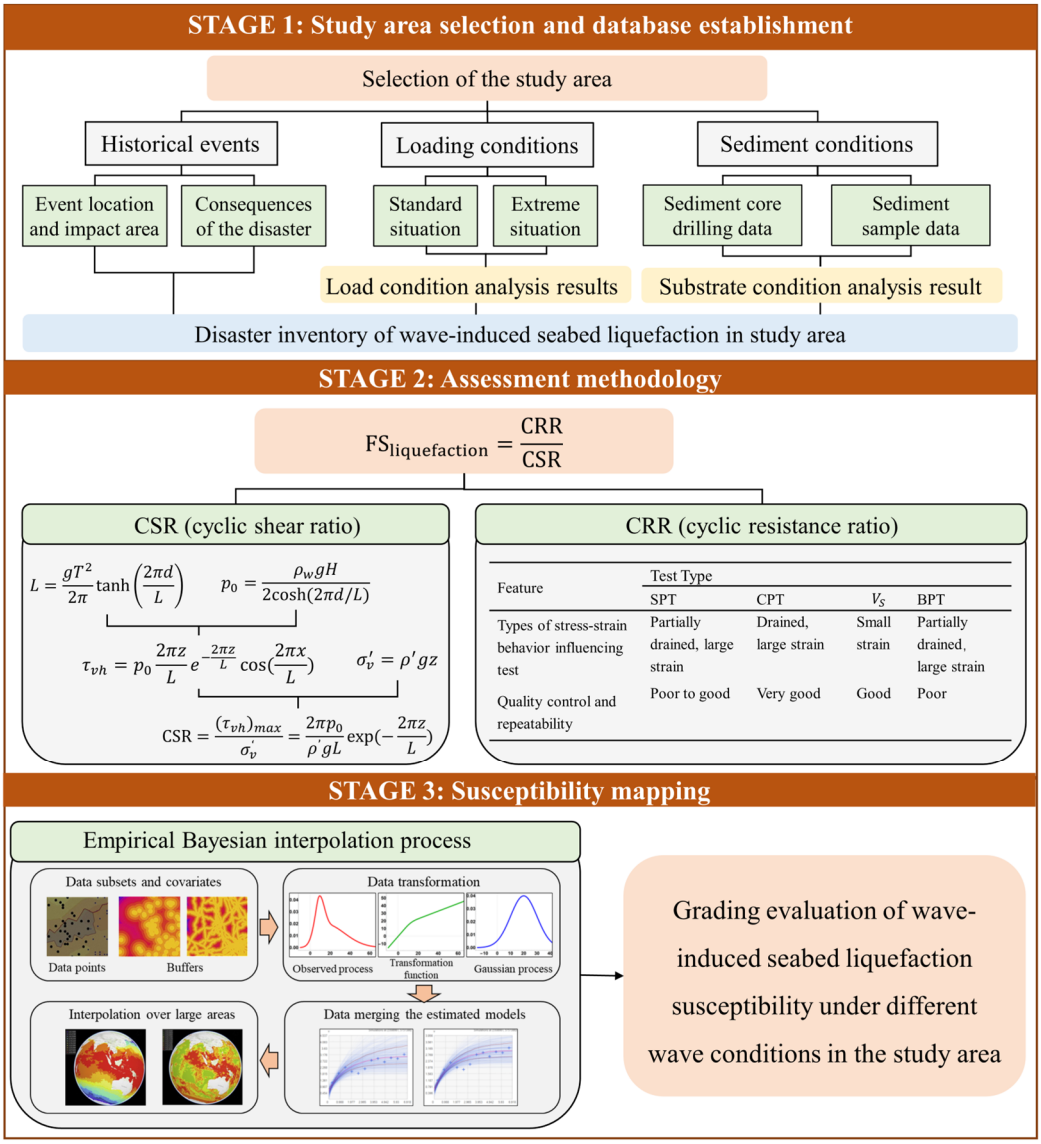

Figure 3. Process for the susceptibility assessment of wave-induced seabed liquefaction (modified from [14,22,43,44]).

This study proceeds through the following steps:

(1) Identify the study area through a comprehensive review of historical data. Summarize the fundamental wave characteristics within this region and establish a comprehensive disaster inventory.

(2) Calculate the CSR of all measurement points using Equation (8), considering the measured water depth and wave parameters of different wave recurrence periods. Utilize the cyclic triaxial torsion shear test data from sampling points to calculate CRR at the known depth of each sampling point. Select the minimum CRR value for each measurement point as the CRR value for susceptibility assessment. Calculate the safety factor of wave-induced seabed liquefaction at the known depth of each sampling point under the different wave conditions by applying Equation (1). Select the minimum safety factor value for each point under varying wave conditions.

(3) Analyze and process the data through ArcGIS 10.7, incorporating interpolation methods to generate a liquefaction susceptibility zoning map for the study area. Subsequently, conduct an in-depth analysis of the zoning results.

3. A Case Study in a Silt-Dominated Nearshore Environment

3.1. Study Area

Numerous studies indicate that nearshore silty seabed are typical areas prone to liquefaction, posing a significant threat to the stability of nearshore marine engineering [7,45–47]. In this context, the Chengdao Island area, where silty sediments are widely distributed, has been selected as the study area. The Chengdao region is situated to the north of the Yellow River Estuary in China, exhibiting a southwest-to-northeast topographical gradient, as depicted in Figure 4. This area primarily consists of two subdeltas [47]. The first subdelta was formed when the Yellow River was redirected to the Shenxiangou flow path from 1953 to 1964, while the second subdelta was established when the river was diverted to the Diaokou flow path from 1964 to 1976 [48]. The underwater Yellow River Estuary spans an area of approximately 3000 km^2. A distinctive feature of this region is its remarkably gentle gradient, typically less than 0.4°, and an exceptionally low slope drop ranging from 1% to 5% [48]. This makes the area highly susceptible to storm surge hazards [1]. Between 1949 and 2005, more than 150 storm surge events occurred in the region, with an average of two to three events per year, of which 36 storm surges caused geological disasters, most of which occurred in the summer and fall [49].

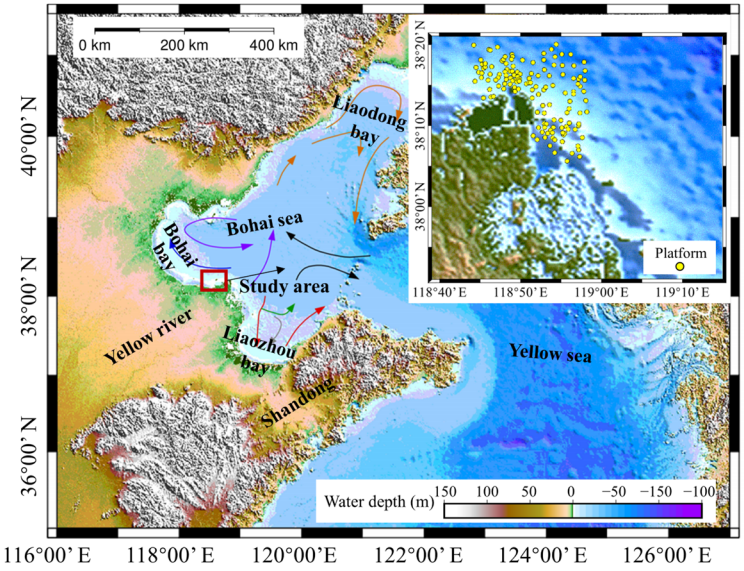

Figure 4. Overview of the Chengdao region and the study zone. The large image shows the location of the Chengdao region and the study zone, with arrows indicating the direction of ocean currents in the study area; the small image in the upper right corner represents the study zone, where yellow indicates the distribution of offshore platforms in existing publicly available data (images modified from Zhang et al. [47] and Wang et al. [50]).

The Chengdao region holds significant engineering importance as it encompasses the Chengdao oil field, which is a crucial oil-producing area. Numerous engineering facilities, including oil platforms, submarine pipelines, and breakwaters, have been established in this region [51–53]. However, the marine engineering environment in the Chengdao region is notably complex, with frequent occurrences of seabed liquefaction leading to numerous destabilization accidents involving offshore engineering facilities. For instance, in November 2003, a seabed deformation sliding event occurred near the oil production platform CB12B, which led to the rupture and interruption of two submarine cables. In May 2009, the CB25A-CB25B subsea crude oil transmission pipeline fractured near the endpoint of CB25A [52]. The investigation data indicated that the accident site was approximately 50–60 m from the CB25A platform, 80 m from the intersection of the Center II-CB1A subsea pipeline, and 200 m from the Center II-CB1A submarine cable. Furthermore, a capsizing incident occurred on the Shengli Operation No. 3 maintenance platform near the CB22C

well group platform of Chengdu Island Oilfield in 2010, putting 36 people in danger [54]. Unfortunately, two individuals lost their lives [7]. The Shengli Operation No. 3 platform and the adjacent seabed were adversely affected by intense wind and waves induced by a typhoon. This led to the liquefaction of the soft substrate beneath the platform, and as the liquefaction zone gradually expanded, it triggered instability, ultimately causing the capsizing of the platform [7].

3.2. Cyclic Stress Ratio under Various Wave Return Periods

The Chengdao region is influenced by prevailing monsoon winds, experiencing dominant north winds in the winter and south winds in the summer [52]. Wave patterns in this area are primarily controlled by surface winds, characterized by short wind zones, rapid wave growth, high wave heights, short wave periods, and limited attenuation distances. These characteristics are associated with the semi-enclosed nature of the Chengdao region, which is connected solely to the Yellow Sea through the narrow Bohai Strait. Furthermore, the engineering geological conditions of the underwater delta impact wave propagation, limiting the distance waves can travel [55]. Under normal sea conditions, wave heights typically do not exceed 1.5 m. However, during extreme sea conditions, wave heights can surpass 5.8 m, and the measured maximum current velocity can reach 1.5 m/s [1]. It is estimated that the extreme water level may increase by 1.8–3.2 m per year, with an average increase of 2.2 m in the Chengdao region [46]. These extreme conditions are primarily generated by weather phenomena such as typhoons, cyclones, and cold waves [56]. Observational and numerical simulation data provide a breakdown of wave information for different wind conditions in the Chengdao region, as shown in Table 3.

Table 3. Corresponding wave elements under different wave recurrence periods in the Chengdao region (data from [46]).

Water Depth	5-Year Return Period			10-Year Return Period			25-Year Return Period		
(m)	$H_{1/10}$ (m)	L (m)	T (s)	$H_{1/10}$ (m)	L (m)	T (s)	$H_{1/10}$ (m)	L (m)	T (s)
3	2.0	42.0	8.0	2.0	42.6	8.1	2.0	44.2	8.4
4	2.6	48.5	8.0	2.6	49.2	8.1	2.6	50.9	8.4
5	3.4	53.9	8.0	3.4	54.5	8.1	3.4	56.6	8.4
6	4.0	58.4	8.0	4.0	58.9	8.1	4.0	61.2	8.4
7	4.3	61.4	8.0	4.6	62.3	8.1	4.6	64.9	8.4
8	4.4	64.9	8.0	4.6	65.8	8.1	4.9	68.7	8.4
9	4.5	65.4	8.0	4.7	68.6	8.1	5.0	71.6	8.4
10	4.6	70.9	8.0	4.8	71.1	8.1	5.1	74.2	8.4
14	5.0	79.9	8.0	5.2	79.2	8.1	5.6	82.8	8.4

Note: $H_{1/10}$ is the effective wave height.

According to linear wave theory, an extreme wave event can be considered to consist of many different waves with characteristics, and the wave components can be characterized by wave period, wavelength, and wave height [31]. The peak wave stress in the study area is calculated under the wave conditions of a 5-year, 10-year, and 25-year return period to analyze the distribution of cyclic stress within the study area across varying wave conditions and sampling depths. Considering that the maximum liquefaction depth in the Chengdao region is less than 15 m, CSRs for three different wave conditions at sampling depths of 5 m, 10 m, and 15 m were further calculated [13]. The interpolation method was utilized to generate a zonal map of the peak wave pressures under different wave conditions ($\rho_w = 1025\ \mathrm{kg/m^3}$ is the density of seawater and $g = 9.8\ \mathrm{m/s^2}$ is the gravitational acceleration), as shown in Figure 5.

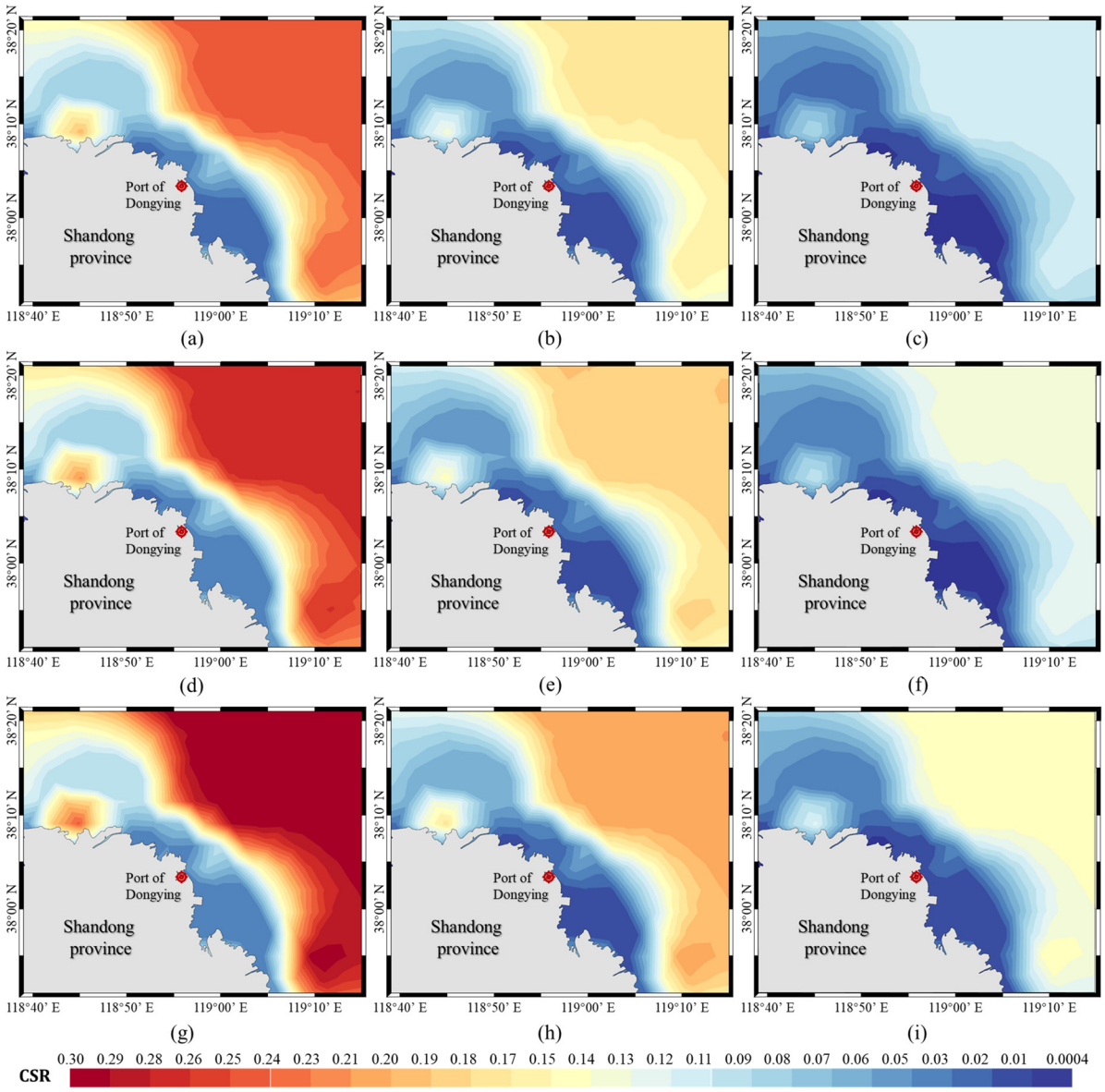

Figure 5. CSR of the study area (the small image in Figure 4) under different wave conditions at different sampling depths: (**a**) CSR of the wave condition in a 5-year return period at 5 m depth; (**b**) CSR of the wave condition in a 5-year return period at 10 m depth; (**c**) CSR of the wave condition in a 5-year return period at 15 m depth; (**d**) CSR of the wave condition in a 10-year return period at 5 m depth; (**e**) CSR of the wave condition in a 10-year return period at 10 m depth; (**f**) CSR of the wave condition in a 10-year return period at 15 m depth; (**g**) CSR of the wave condition in a 25-year return period at 5 m depth; (**h**) CSR of the wave condition in a 25-year return period at 10 m depth; and (**i**) CSR of the wave condition in a 25-year return period at 15 m depth.

Overall, a discernible spatial regularity characterizes the distribution of CSR, with contours closely aligned with the coastline. The lowest CSR value is observed under the wave conditions of a 5-year return period, situated at a depth of 15 m in the southeastern offshore area of the study region, with a value of 0.0004. Conversely, the highest CSR value is found under the wave conditions of a 25-year return period, located at a depth of 5 m in the northeastern offshore area, with a value of 0.305. A deeper analysis of the CSR distribution at different depths but the same wave conditions reveals a general increasing trend from nearshore to offshore areas. However, a distinct spatial pattern emerges in the northern nearshore part of the Chengdao region, characterized by a concentration of higher CSR values where numerous offshore platforms are located. Additionally, CSR displays a

negative correlation with sampling depth, ranging from 0.03 to 0.31 at 5 m depth, 0.01 to 0.23 at 10 m depth, and 0.0004 to 0.16 at 15 m depth. This indicates that deeper sediment experiences a reduced impact from wave loading. By analyzing the distribution of CSR at the same depth but under different wave conditions, it can be found that higher wave conditions lead to an increased CSR, which, in turn, amplifies the likelihood of seabed liquefaction. The precision of the interpolation results is primarily attributed to the limited distribution of interpolation points. However, regarding the interpolation of CSR, the known data points are mostly distributed in nearshore areas, with fewer points in offshore areas. As a result, the accuracy of interpolation results in offshore areas will be lower than in nearshore areas.

3.3. Cyclic Resistance Ratio of Sediments

The sediment types in the Chengdao region can be categorized into four types, including clay, silty clay, silt, and silty sand, as shown in Figure 6 [52]. In the Chengdao oil field beach and shallow marine stratigraphy, silt is the main sediment type [51]. However, the nearshore area experiences strong hydrodynamic forces and sediment redeposition, leading to a more intricate sediment composition [49]. This results in an alternation between coarser and finer sediment types, with silt predominating locally. Moreover, the distribution of silt in the far shore area slightly surpasses that of clay [46,57].

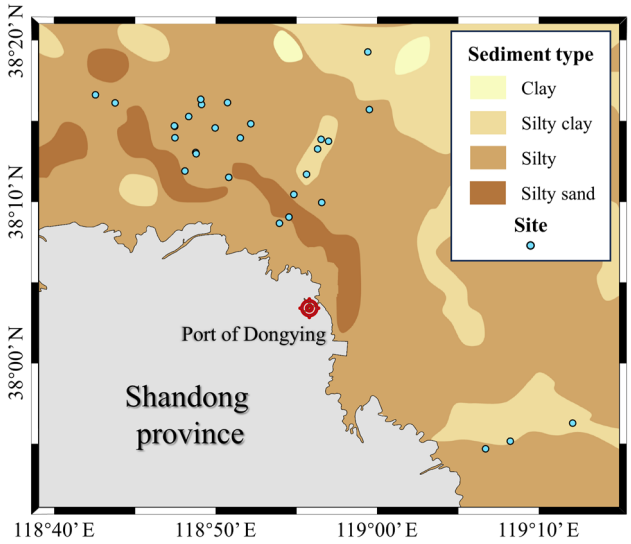

Figure 6. Distribution of sediment types in the study area. Blue dots represent sample points (data from Liu et al. [51] and Liu et al. [52]).

The sediment strength in the Chengdao region exhibits a notable pattern, which can be observed in Figure 7, depicting the distribution of undrained shear strength in depth ranges of 0–5 m, 5–10 m, and 10–15 m. The exact calculation results are presented in Appendix A. Because of more rapid sedimentation, the shallow sediments usually do not reach complete consolidation, so their undrained shear strengths are lower, and the range of variation is smaller [57]. On the contrary, the undrained shear strength of the deeper sediments roughly shows a gradual increase along the delta and outward [57]. This phenomenon results from a gradual reduction in sedimentation rates and a progressive thinning of sediment particles. Furthermore, regional trends in the sediment water content, the pore ratio, and the liquid–plastic limit follow a similar pattern, with these parameters gradually increasing with water depth and distance from the Diaokou inlet [48]. These characteristics collectively create conditions characterized by low consolidation, a high water content, a high pore ratio, and low strength, which increases the risk of geological disasters such as sliding, thixotropy, and liquefaction.

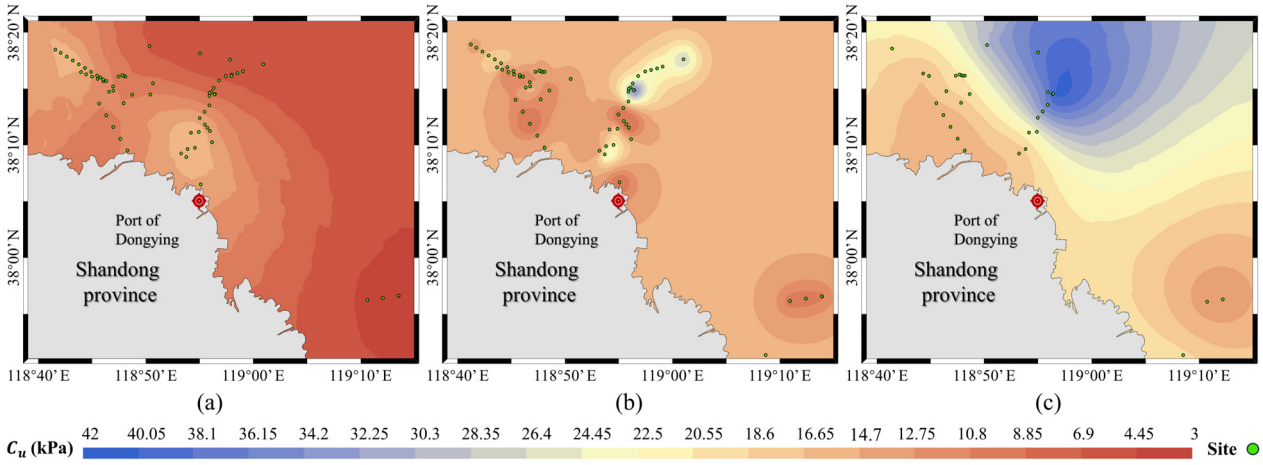

Figure 7. Distribution of undrained shear strength in the Chengdao region at different sampling depths of 0–5 m (**a**), 5–10 m (**b**), and 10–15 m (**c**).

To calculate CRR, this study used the cyclic triaxial shear test data. The method for this experiment was the consolidation of undrained shear, with an isotropic consolidation process (i.e., axial consolidation pressure (σ_1) equaled lateral consolidation pressure (σ_3)). After consolidation was completed, the confining pressure and axial pressure remained unchanged, while a sinusoidal axial load with a frequency of 1 Hz was applied. This caused cyclic shear stress on a 45° inclined plane within the soil sample, simulating the shear forces induced by wave loading within the seabed. The same set of soil samples was subjected to at least three different amplitudes of dynamic loading to obtain a relationship curve between the number of cycles and the dynamic stress ratio. Data from 29 groups of cyclic triaxial tests conducted between 1998 and 2017 with sediment samples in the study area were collected and organized. The relationship between the dynamic stress ratio and the number of cycles at various depths was fitted to calculate the cyclic resistance ratio (CRR) for each sampling point. The exact calculation results are provided in Appendix B. The minimum CRR value at each point was selected as the final CRR. Figure 8 only presents the relationship between the dynamic stress ratio and the number of cycles for a portion of different sampling points, along with the method for determining CRR. However, because of the nonuniform distribution of 29 sampling points, it was necessary to utilize Empirical Bayesian Interpolation to extrapolate the CRR distribution across the continuous surface of the study area, as illustrated in Figure 9.

CRR mainly reflects the ability of sediments in the study area to resist liquefaction. In general, variations in CRR within the study area are relatively minor and closely linked to sediment type. The northwestern region predominantly features silt sediments, with most of this area exhibiting CRR values exceeding 0.27, indicating greater resistance to liquefaction. Furthermore, CRR correlates with undrained shear strength, which is notably lower in the southeastern region at different depths, resulting in a CRR within the range of 0.2 to 0.22. Unlike the distribution of CSR, CRR does not follow a coastline-based distribution pattern. Instead, they display one high CRR center and three low CRR centers arranged in a concentric circle formation. These interpolation results are influenced by the distribution of sampling points and the selection of the interpolation method.

A comprehensive analysis of CSR, CRR, and safety factors at various sampling depths at the same location reveals interesting patterns. Under the same wave condition, CSR and CRR exhibit a gradual decrease as sampling depth increases. The reduction in CSR (Figure 5) is associated with the attenuation of stress as waves propagate downward through the sediment layers. Furthermore, the reduction in the CRR trend could be attributed to the robust hydrodynamic forces in the nearshore area, which generate intense shear stresses, inhibiting the settling of sediment particles toward the seabed and consequently resulting in a decline in CRR with greater depth. However, as sampling depth increases, the magnitude

of reduction in CSR surpasses that of CRR, resulting in an increase in the safety factor and a decreased susceptibility to wave-induced seabed liquefaction. This implies that the depth of sediment may significantly influence the susceptibility to wave-induced seabed liquefaction, leading to a reduced susceptibility to disasters.

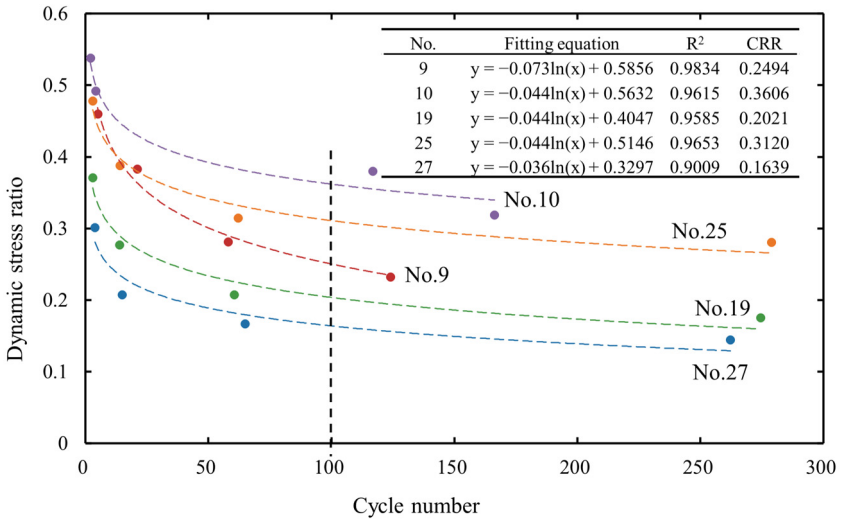

Figure 8. The relationship between the dynamic stress ratio of the selected sampling points and the number of cycles. The dotted line represents the dynamic stress ratio corresponding to the cycle number of 100, which is considered the CRR of the sampling point.

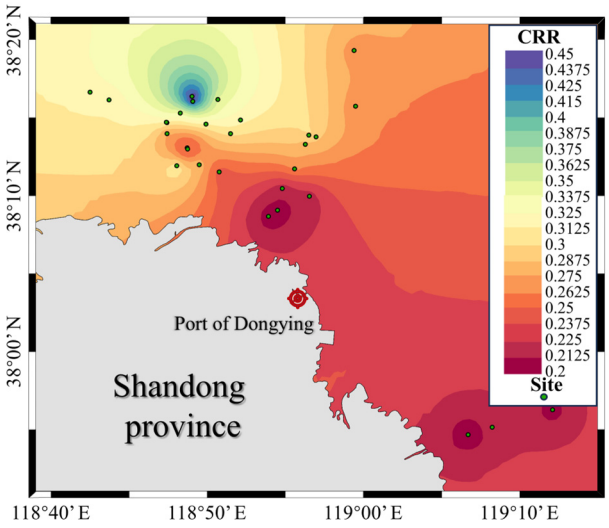

Figure 9. The interpolated distribution represents the minimum values of known CRRs for the sampling points within the 15 m depth range.

3.4. Susceptibility Assessment

The safety factor for wave-induced seabed liquefaction at various known depths of sampling points was calculated following the previously outlined procedure. These calculations were conducted under different wave conditions corresponding to 5-year, 10-year, and 25-year return periods. We considered the smallest safety factor among those calculated at different known depths as the safety factor for wave-induced seabed liquefaction at that specific point, as detailed in Table 4. Subsequently, we utilized EBK in ArcGIS 10.7 to generate a distribution map of the safety factor of wave-induced seabed liquefaction, as shown in Figure 10.

Table 4. CSRs, CRRs, and the safety factor minima calculated for 29 core sampling points.

No.	Latitude (N)	Longitude (E)	Sampling Depth (m)	CSR-5y	CSR-10y	CSR-25y	CRR	FS-5y	FS-10y	FS-25y
1	38°09′52″	118°56′33″	12.5	0.0965	0.1022	0.1161	0.1836	1.9023	1.7960	1.5809
2	38°11′26″	118°50′48″	3	0.0951	0.1031	0.1069	0.1948	2.0477	1.8904	1.8220
3	38°16′32″	118°42′33″	5	0.1148	0.1213	0.1337	0.3379	2.9431	2.7853	2.5262
4	38°16′02″	118°43′45″	10	0.0641	0.0684	0.0772	0.3031	4.7245	4.4323	3.9275
5	38°15′12″	118°48′18″	15	0.0211	0.0218	0.0238	0.3151	14.9494	14.4820	13.2178
6	38°13′47″	118°56′31″	3	0.2702	0.2962	0.3299	0.3605	1.3339	1.2171	1.0926
7	37°56′13″	119°12′04″	9	0.1860	0.2087	0.2327	0.1792	0.9631	0.8586	0.7699
8	38°10′22″	118°54′49″	4.2	0.1544	0.1685	0.1799	0.1697	1.0989	1.0066	0.9433
9	38°15′38″	118°59′30″	8	0.2001	0.2241	0.2491	0.2494	1.2466	1.1128	1.0015
10	38°14′35″	118°47′27″	2.3	0.0645	0.0642	0.0668	0.3606	5.5879	5.6146	5.3979
11	38°14′45″	118°52′09″	5	0.1148	0.1213	0.1337	0.3314	2.8872	2.7325	2.4783
12	38°13′53″	118°51′31″	5	0.1018	0.1078	0.1193	0.3250	3.1923	3.0155	2.7243
13	38°12′58″	118°48′44″	12	0.0114	0.0118	0.0129	0.1121	9.8112	9.5096	8.6919
14	38°15′56″	118°49′06″	4	0.0985	0.1043	0.1155	0.6891	6.9947	6.6040	5.9662
15	38°16′16″	118°49′03″	7	0.0737	0.0784	0.0878	0.7281	9.8829	9.2914	8.2944
16	37°55′07″	119°08′13″	9	0.1740	0.1921	0.2187	0.2288	1.3151	1.1907	1.0461
17	38°13′53″	118°47′28″	2	0.0423	0.0429	0.0447	0.2204	5.2083	5.1376	4.9361
18	38°11′49″	118°48′05″	2	0.1196	0.1263	0.1387	0.4844	4.0513	3.8358	3.4931
19	38°12′54″	118°48′46″	3.1	0.0366	0.0372	0.0380	0.2020	5.5149	5.4297	5.3092
20	38°11′38″	118°55′36″	6.3	0.2101	0.2323	0.2619	0.3528	1.6788	1.5184	1.3475
21	38°13′40″	118°56′58″	14	0.1292	0.1459	0.1657	0.3082	2.3848	2.1123	1.8604
22	38°16′04″	118°50′43″	5	0.1148	0.1213	0.1337	0.3299	2.8741	2.7201	2.4670
23	38°14′37″	118°47′25″	5	0.0457	0.0477	0.0491	0.5014	10.9623	10.5121	10.2190
24	38°14′29″	118°49′57″	10	0.0364	0.0373	0.0400	0.3103	8.5222	8.3192	7.7590
25	38°13′11″	118°56′17″	3.6	0.2580	0.2829	0.3166	0.3120	1.2032	1.1027	0.9853
26	37°54′38″	119°06′41″	4	0.1794	0.1987	0.2185	0.1669	0.9300	0.8397	0.7635
27	38°08′35″	118°53′56″	8	0.0328	0.0336	0.0359	0.1639	4.9898	4.8789	4.5715
28	38°08′59″	118°54′31″	10	0.0259	0.0266	0.0286	0.1884	7.2663	7.0817	6.5748
29	38°19′12″	118°59′24″	5	0.2489	0.2778	0.3054	0.2455	0.9860	0.8835	0.8038

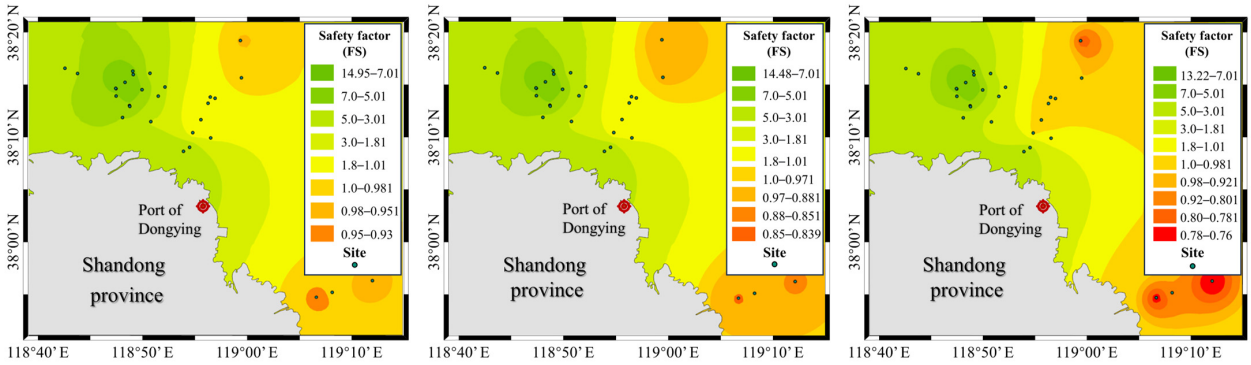

Figure 10. Grading evaluation of wave-induced seabed liquefaction susceptibility in the Chengdao region under wave conditions in a 5-year return period (**a**), a 10-year return period (**b**), and a 25-year return period (**c**), respectively.

Figure 10 reveals the susceptibility assessment result of wave-induced seabed liquefaction in the Chengdao region. The zoning of susceptibility refers to previous research by Chang et al. [48]. The safety factor and liquefaction probability of sediments against liquefaction were calculated under different wave conditions, taking into account the variability in wave and soil parameters. Based on the Chengdao region, a division of the safety factor was proposed. If the probability is controlled within 5%, the safety factor must be greater than 1.8, i.e., the area is a non-liquefaction zone when FS > 1.8 and a liquefaction susceptibility zone when FS < 1.8 [48]. Broadly, the safety factor in the western part of the study area surpasses that in the eastern part, showing substantial spatial variation. The extent of the susceptibility zone expands with more severe wave conditions. Under the wave condition in a 5-year return period, the safety factor in the study area ranges from 0.93

to 14.95, with the liquefaction susceptibility zone encompassing 64.46% of the total study area. Under the wave condition in a 10-year return period, the safety factor ranges from 0.839 to 14.48, covering 65.07% of the study area. Under the wave condition in a 25-year return period, the safety factor varies from 0.76 to 13.22, with the susceptibility zone encompassing 68.89% of the study area. The distribution of the safety factor shows a concentric circle structure centered on the sampling point, with a high safety factor center occurring in the northwestern area and a low safety factor center in the southeastern area. The high safety factor center was located in the northeast of the study area, and its range gradually expanded and developed significantly with an enhancement in wind and wave action, while the range of the high safety factor center in the northwest gradually decreased and the range of the low safety factor center in the southeast gradually expanded (Figure 10). Notably, the safety factor in the western part of the study area under the 25-year return period wave conditions ranges between 0.98 and 1.0. There is an area extending southwestward along the sampling points, and its range changes most significantly, from 18.73% for the wave condition in a 5-year return period to 43.11% for the wave condition in a 25-year return period. Combining the distribution of sampling points and susceptibility areas, it is observed that most sampling points are located in high-safety areas. However, there are still some sampling points with lower safety factors. This is of concern because some important submarine engineering facilities are in these zones. For example, submarine cables from KD48 to KD34C, near borehole K1-1, are buried in an area with the lowest safety factor. This site is particularly susceptible to wave-induced seabed liquefaction under different wave conditions.

The method can realize the preliminary susceptibility assessment of wave-induced seabed liquefaction, which provides a reference value for the construction of marine engineering and maintenance of facilities, but there remains room for its enhancement. Firstly, the accuracy of susceptibility assessments in areas with limited or sparse data points is compromised because of their spatial distribution and the lack of data. Secondly, the current method does not fully account for the influence of sampling depth changes on the safety factor, making it unable to provide a comprehensive assessment of the three-dimensional spatial susceptibility to wave-induced seabed liquefaction. Consequently, the evaluation results may deviate from the actual conditions. To enhance the accuracy of this method, future research can explore wave-induced seabed liquefaction principles through extensive indoor experiments, take into account the impact of sampling depth on susceptibility more comprehensively, and potentially employ machine learning-based models to achieve a more precise evaluation. These improvements could lead to more reliable results in evaluating susceptibility and better support marine engineering construction and facility maintenance decisions.

4. Conclusions

This study modifies the formula for calculating the safety factor, which makes the method suitable for studying the susceptibility assessment of seafloor sediment liquefaction under wave loads. This method employs the safety factor as a primary evaluation criterion and combines an analysis of the cyclic stress ratio (CSR) and the cyclic resistance ratio (CRR) to provide a comprehensive assessment. The Chengdao region in China, characterized by extensive silt distribution, was selected as the study area. To create a regional evaluation zoning map for the susceptibility of wave-induced seabed liquefaction, Empirical Bayesian Kriging (EBK) in the Arc Geographic Information System 10.7 (ArcGIS 10.7) was utilized. The following conclusions can be drawn from this study:

(1) A method for the susceptibility assessment of wave-induced seabed liquefaction was modified using the safety factor. This safety factor was determined by employing CSR to account for the wave characteristics in the study area and CRR to reflect the sediment properties. This method was then applied to the Chengdao region, where a substantial amount of data was collected to evaluate the susceptibility of wave-induced seabed liquefaction. The EBK method was further utilized to create zoning

maps for the susceptibility assessment of wave-induced seabed liquefaction in the Chengdao region under varying wave conditions.

(2) CSR primarily characterizes the wave conditions in the study area and is a crucial factor for the susceptibility assessment of wave-induced seabed liquefaction. In this study, CSR values are calculated using basic wave elements based on linear wave theory. To gain a deeper insight into the impact of waves on the susceptibility assessment of wave-induced seabed liquefaction and enhance the accuracy of the evaluation, we believe that multiple extreme wave conditions should be calculated for CSR.

(3) CRR primarily represents the sediment characteristics of the study area, and its calculation method should be tailored to the sediment types in the study area. This study presents several testing methods, such as SPT (Standard Penetration Test), CPT (Cone Penetration Test), measurement of V_S (shear wave velocity), and BPT, with a specific focus on the cyclic triaxial test, which is convenient for rapid computation, and the data are easily obtainable, making it applicable to various types of sediments.

(4) The safety factor serves as an effective indicator of wave-induced seabed liquefaction susceptibility assessment in the study area. The safety factor integrates the wave characteristics and sediment properties of the study area. Combined with spatial interpolation methods, it allows for a continuous assessment of wave-induced seabed liquefaction susceptibility across the study area. The specific categorization of susceptibility levels also needs to consider the characteristics of the study area and liquefaction probabilities. Through the calculation of safety factors, it was observed that CSR is more sensitive to changes in sampling depth compared with CRR, exerting a greater impact on the safety factor. Therefore, in future studies, it is crucial to consider the sampling depth as a key reference factor for a more comprehensive evaluation of wave-induced seabed liquefaction susceptibility in three-dimensional space.

Overall, the methodology of this study provides a tool for the susceptibility assessment of wave-induced seabed liquefaction, setting the stage for subsequent risk assessment of such disasters. This method can be directly applied to seabed areas in the study region where the sediment type is silt, providing a spatial reference for stability assessment and site selection of marine engineering facilities within the study area. When this method is applied to other types of sediment in the study area, the formula of the cyclic resistance ratio needs to be adjusted according to the characteristics of the sediment. However, we also need to recognize that there is still room for improvement in this method, especially in the amount and distribution of data, and more in-depth studies are needed to enhance the accuracy and reliability of the assessment.

Author Contributions: Conceptualization, Y.W., X.G. and X.L.; methodology, Y.W. and X.G.; software, Y.W.; formal analysis, J.L. and F.H.; investigation, J.L. and F.H.; resources, J.L. and F.H.; data curation, J.L. and F.H.; writing—original draft preparation, Y.W. and H.G.; writing—review and editing, Y.W., X.G., H.Z. and X.L.; visualization, H.G.; funding acquisition, X.G., H.Z. and X.L. All authors have read and agreed to the published version of the manuscript.

Funding: This research was financially supported by the Fundamental Research Funds for the Central Universities (202441003), the National Natural Science Foundation of China (42207181), the Shandong Province National-Level Leading Talent Supporting Project (2022GJJLJRC-15), the Opening Fund of the State Key Laboratory of Geohazard Prevention and Geoenvironment Protection at Chengdu University of Technology (SKLGP2023K001), and the Shandong Provincial Key Laboratory of Ocean Engineering with grant at Ocean University of China (kloe202301).

Institutional Review Board Statement: Not applicable.

Informed Consent Statement: Not applicable.

Data Availability Statement: All data, models, and code generated or used during this study appear in this submitted article.

Acknowledgments: We are indebted to the National Resource Sharing Service Platform—National Marine Science Data Center for furnishing the 2018 annual wave element data for the Chengdao area. We acknowledge with gratitude the provision of cyclic triaxial test data from the sampling points, the comprehensive physical and mechanical property data of sediment in the Chengdao area by the Sinopec Petroleum Engineering Corporation, conducted in collaboration with Ocean University of China, the First Institute of Oceanography, Ministry of Natural Resources, Qingdao Huanhai Marine Engineering Survey Institute, and Sinopec Petroleum Engineering Corporation. Additionally, we would like to extend our appreciation to Mengjiao Liu for her invaluable assistance in the design and production of the figures.

Conflicts of Interest: Jinkun Liu and Fang Hou were employed by the Sinopec Petroleum Engineering Corporation. The remaining authors declare that the research was conducted in the absence of any commercial or financial relationships that could be construed as a potential conflict of interest.

Abbreviations and Symbols

C_u	undrained shear strength
D_r	relative density
K_0	coefficient of earth pressure at rest
M_w	earthquake moment magnitude
$N_{1,60}$	standard penetration test blowcount value corrected for overburden, energy, equipment, and procedural factors
P_L	probability of triggering of liquefaction
P_a	atmospheric pressure (1 atm)
R_f	friction ratio
V_s	shear wave velocity
V_{s1}	effective stress normalized shear-wave velocity
p_0	amplitude of the pressure fluctuation exerted on the sea bottom
$q_{c,1}$	normalized cone tip resistance
θ_i	set of unknown model coefficients
ρ'	submerged unit mass of soils in the seabed
ρ_w	density of seawater
σ_1	axial consolidation pressures
σ_3	lateral consolidation pressures
σ_h	horizontal normal stress
σ_C	average consolidation pressures
σ_d	cyclic dynamic stress
σ'_v	vertical effective stress
τ_L	horizontal shear stress
τ_{vh}	shear stress
ArcGIS	Arc Geographical Information System
ASCE	American Society of Civil Engineers
BPT	Becker Penetration Test
CPT	Cone Penetration Test
CRR	cyclic resistance ratio
CSR	cyclic stress ratio
EBK	Empirical Bayesian Kriging
FC	fines content
FS	safety factor
NSW	nearshore spectral windwave
SASW	Spectral Analysis of Surface Waves Method
SPT	Standard Penetration Test
z	sampling depth
$H_{1/10}$	effective wave height
Φ	standard cumulative normal distribution
H	wave height
L	wave length
N	number of cyclic loadings
T	wave period

d	water depth
g	gravitational acceleration
k	wave number
t	time coordinate
ω	wave frequency

Appendix A. Data on Undrained Shear Strength (C_u)

Table A1. The mean undrained shear strength of sediments in the range of 0–5 m.

No.	Longitude (E)	Latitude (N)	C_u (kPa)	No.	Longitude (E)	Latitude (N)	C_u (kPa)	No.	Longitude (E)	Latitude (N)	C_u (kPa)
1	38°11′37.527″	118°55′36.164″	8.98	24	38°11′37.527″	118°55′36.164″	13.79	46	38°13′31.550″	118°56′28.545″	8.50
2	38°13′58.479″	118°47′50.427″	31.00	25	38°13′40.223″	118°56′58.128″	10.64	47	38°14′51.026″	118°57′20.382″	7.50
3	38°14′35.813″	118°51′24.383″	9.50	26	38°15′37.895″	118°59′29.534″	4.89	48	38°15′28.451″	118°58′59.854″	7.83
4	38°13′38.735″	118°51′10.270″	22.50	27	38°8′35.324″	118°53′55.815″	6.67	49	38°15′21.194″	118°58′28.706″	9.67
5	38°15′11.221″	118°48′55.427″	6.25	28	38°8′58.727″	118°54′31.065″	9.67	50	38°15′13.898″	118°57′57.407″	9.00
6	38°15′14.378″	118°48′47.141″	7.33	29	38°12′51.577″	118°46′33.851″	16.13	51	38°14′47.305″	118°47′12.758″	23.00
7	38°15′17.532″	118°48′38.830″	7.67	30	38°11′51.329″	118°47′11.960″	10.57	52	38°15′06.877″	118°46′40.886″	23.00
8	38°15′11.792″	118°48′18.430″	17.50	31	38°10′51.110″	118°47′50.093″	7.093	53	38°14′55.867″	118°46′55.874″	20.33
9	38°13′52.956″	118°47′27.762″	10.00	32	38°9′50.856″	118°48′28.209″	8.79	54	38°15′15.444″	118°46′23.098″	23.25
10	38°13′38.289″	118°49′32.524″	8.00	33	38°8′51.122″	118°49′05.992″	10.83	55	38°15′35.003″	118°45′50.350″	16.00
11	38°15′22.392″	118°45′24.160″	6.50	34	38°10′31.501″	118°56′31.520″	13.50	56	38°15′54.592″	118°45′17.536″	20.33
12	38°15′10.623″	118°45′54.851″	6.50	35	38°10′48.020″	118°56′17.790″	12.33	57	38°16′14.163″	118°44′44.746″	22.25
13	38°14′58.852″	118°46′25.540″	5.50	36	38°11′04.538″	118°56′04.057″	18.67	58	38°16′33.734″	118°44′11.951″	24.67
14	38°14′47.079″	118°46′56.226″	4.50	37	38°5′56.911″	118°55′41.783″	17.33	59	38°16′53.283″	118°43′39.146″	18.00
15	38°14′20.103″	118°47′48.698″	5.00	38	37°56′24.973″	119°13′28.386″	3.00	60	38°17′12.862″	118°43′06.349″	12.00
16	38°10′26.026″	118°55′31.334″	25.00	39	37°56′23.958″	119°13′29.568″	4.50	61	38°17′29.534″	118°42′38.384″	11.00
17	38°9′05.299″	118°55′10.320″	16.50	40	37°56′13.302″	119°12′04.466″	4.25	62	38°12′53.977″	118°48′46.351″	8.75
18	38°8′17.413″	118°54′23.899″	32.5	41	37°56′01.755″	119°10′40.617″	4.33	63	38°17′47.306″	118°51′05.372″	4.83
19	38°12′42.606″	118°56′28.897″	14.75	42	38°9′33.488″	118°56′42.908″	10.00	64	38°17′10.451″	118°55′38.071″	3.45
20	38°13′47.422″	118°56′30.587″	4.87	43	38°15′33.877″	118°44′55.901″	22.49	65	38°16′38.159″	118°58′19.233″	3.46
21	38°12′10.039″	118°56′02.593″	17.18	44	38°14′13.013″	118°56′51.961″	9.00	66	38°16′14.429″	119°1′19.094″	4.82
22	38°10′22.429″	118°54′48.940″	31.17	45	38°13′52.281″	118°56′40.254″	8.67	67	38°15′14.770″	118°58′28.480″	4.15
23	38°13′38.989″	118°56′56.266″	7.36								

Table A2. The mean undrained shear strength of sediments in the range of 5–10 m.

No.	Longitude (E)	Latitude (N)	C_u (kPa)	No.	Longitude (E)	Latitude (N)	C_u (kPa)	No.	Longitude (E)	Latitude (N)	C_u (kPa)
1	38°11′37.527″	118°55′36.164″	5.24	22	38°10′22.429″	118°54′48.940″	13.61	43	38°15′33.877″	118°44′55.901″	23.60
2	38°13′58.479″	118°47′50.427″	22.80	23	38°13′38.989″	118°56′56.266″	36.38	44	38°14′13.013″	118°56′51.961″	26.00
3	38°14′35.813″	118°51′24.383″	13.00	24	38°11′37.527″	118°55′36.164″	9.380	45	38°13′52.281″	118°56′40.254″	23.13
4	38°15′11.661″	118°49′07.406″	17.00	25	38°15′37.895″	118°59′29.534″	22.70	46	38°13′31.550″	118°56′28.545″	26.00
5	38°15′11.221″	118°48′55.427″	8.73	26	38°8′35.324″	118°53′55.815″	9.67	47	38°14′51.026″	118°57′20.382″	21.38
6	38°10′26.026″	118°55′31.334″	25.00	27	38°8′58.727″	118°54′31.065″	18.00	48	38°15′28.451″	118°58′59.854″	26.00
7	38°15′14.378″	118°48′47.141″	13.00	28	38°12′51.577″	118°46′33.851″	11.80	49	38°15′21.194″	118°58′28.706″	23.88
8	38°15′17.532″	118°48′38.830″	12.75	29	38°11′51.329″	118°47′11.960″	9.62	50	38°15′13.898″	118°57′57.407″	21.50
9	38°15′11.792″	118°48′18.430″	16.00	30	38°10′51.110″	118°47′50.093″	5.44	51	38°14′47.305″	118°47′12.758″	8.33
10	38°13′52.956″	118°47′27.762″	13.67	31	38°9′50.856″	118°48′28.209″	12.81	52	38°14′55.867″	118°46′55.874″	14.40
11	38°13′38.289″	118°49′32.524″	10.25	32	38°8′51.122″	118°49′05.992″	14.40	53	38°15′15.444″	118°46′23.098″	14.75
12	38°15′22.392″	118°45′24.160″	9.50	33	38°10′31.501″	118°56′31.520″	6.50	54	38°15′35.003″	118°45′50.350″	16.75
13	38°15′10.623″	118°45′54.851″	7.50	34	38°10′48.020″	118°56′17.790″	4.50	55	38°15′54.592″	118°45′17.536″	19.00
14	38°14′58.852″	118°46′25.540″	11.67	35	38°11′04.538″	118°56′04.057″	6.00	56	38°16′14.163″	118°44′44.746″	15.00
15	38°14′47.079″	118°46′56.226″	10.17	36	38°5′56.911″	118°55′41.783″	6.00	57	38°16′33.734″	118°44′11.951″	17.75
16	38°14′20.103″	118°47′48.698″	8.50	37	37°56′24.973″	119°13′28.386″	9.00	58	38°16′53.283″	118°43′39.146″	16.00
17	38°9′05.299″	118°55′10.320″	23.50	38	37°56′23.958″	119°13′29.568″	10.50	59	38°17′12.862″	118°43′06.349″	12.00
18	38°8′17.413″	118°54′23.899″	35.00	39	37°56′13.302″	119°12′04.466″	8.50	60	38°17′29.534″	118°42′38.384″	14.67
19	38°12′42.606″	118°56′28.897″	24.50	40	37°56′01.755″	119°10′40.617″	8.50	61	38°12′53.977″	118°48′46.351″	10.00
20	38°13′47.422″	118°56′30.587″	32.58	41	37°51′30.354″	119°8′32.770″	14.00	62	38°16′14.429″	119°1′19.094″	35.78
21	38°12′10.039″	118°56′02.593″	10.77	42	38°9′33.488″	118°56′42.908″	15.50				

Table A3. The mean undrained shear strength of sediments in the range of 10–15 m.

No.	Longitude (E)	Latitude (N)	C_u (kPa)	No.	Longitude (E)	Latitude (N)	C_u (kPa)	No.	Longitude (E)	Latitude (N)	C_u (kPa)
1	38°11′37.527″	118°55′36.164″	32.54	10	38°15′22.392″	118°45′24.160″	13.25	19	38°11′51.329″	118°47′11.960″	11.65
2	38°15′11.661″	118°49′07.406″	20.00	11	38°15′10.623″	118°45′54.851″	25.00	20	38°10′51.110″	118°47′50.093″	13.22
3	38°15′11.221″	118°48′55.427″	13.00	12	38°10′26.026″	118°55′31.334″	43.00	21	38°9′50.856″	118°48′28.209″	16.17
4	38°15′14.378″	118°48′47.141″	25.00	13	38°12′42.606″	118°56′28.897″	12.15	22	38°8′51.122″	118°49′05.992″	11.00
5	38°15′17.532″	118°48′38.830″	22.50	14	38°13′47.422″	118°56′30.587″	16.70	23	37°56′13.302″	119°12′04.466″	11.00
6	38°15′11.792″	118°48′18.430″	24.50	15	38°10′22.429″	118°54′48.940″	12.00	24	37°56′01.755″	119°10′40.617″	25.67
7	38°13′52.956″	118°47′27.762″	30.00	16	38°8′35.324″	118°53′55.815″	20.00	25	37°51′30.354″	119°8′32.770″	22.00
8	38°13′38.289″	118°49′32.524″	19.00	17	38°8′58.727″	118°54′31.065″	14.87	26	38°17′29.534″	118°42′38.384″	17.50
9	38°11′37.527″	118°55′36.164″	14.00	18	38°12′51.577″	118°46′33.851″	15.60	27	38°12′53.977″	118°48′46.351″	40.00

Appendix B. Data on CRR

Table A4. Sediment cyclic triaxial torsion shear test data in the research area and CRR.

No.	Longitude (E)	Latitude (N)	Lateral Consolidation Pressures (kPa) (σ3′)	Sampling Depth	Cycle Number	Dynamic Stress Ratio	Fitting Formula	R^2	CRR
1	38°09′52.4517″	118°56′32.8744″	125	12.5	8 13 24 68	0.2261 0.2294 0.2120 0.1898	y = −0.019ln(x) + 0.2711	0.925	0.1836
2	38°11′25.8671″	118°50′47.5194″	30	3	1 50 1495	0.2617 0.2104 0.1540	y = −0.015ln(x) + 0.2639	0.9952	0.1948
3	38°16′32.3239″	118°42′32.5437″	50	5	11 56 205	0.4450 0.3560 0.3080	y = −0.047ln(x) + 0.5543	0.9888	0.3379
4	38°16′02.2446″	118°43′45.4653″	100	10	30 76 1366	0.3320 0.3190 0.2340	y = −0.027ln(x) + 0.4274	0.9873	0.3031
5	38°15′11.7918″	118°48′18.4296″	150	15	1 12 1283	0.3240 0.3186 0.3066	y = −0.002ln(x) + 0.3243	0.9983	0.3151
6	38°13′47.4217″	118°56′30.5870″	30	3	6 25 56	0.5877 0.4942 0.3916	y = −0.082ln(x) + 0.7381	0.9609	0.3605
7	37°56′13.3016″	119°12′04.4655″	90	9	1 48 1434	0.3005 0.2041 0.1035	y = −0.027ln(x) + 0.3035	0.9975	0.1792
8	38°10′22.4291″	118°54′48.9404″	42	4.2	7 13 31	0.5548 0.4721 0.3323	y = −0.145ln(x) + 0.8374	0.9913	0.1697
9	38°15′37.8945″	118°59′29.5341″	80	8	5 21 58 124	0.4600 0.3830 0.2810 0.2330	y = −0.073ln(x) + 0.5856	0.9834	0.2494

Table A4. *Cont.*

No.	Longitude (E)	Latitude (N)	Lateral Consolidation Pressures (kPa) (σ3′)	Sampling Depth	Cycle Number	Dynamic Stress Ratio	Fitting Formula	R^2	CRR
10	38°14′35.2878″	118°47′26.9503″	20	2.3	2 4 117 166	0.5379 0.4920 0.3797 0.3186	y = −0.044ln(x) + 0.5632	0.9615	0.3606
11	38°14′44.8627″	118°52′08.9572″	50	5	232 254 2143	0.3100 0.3000 0.2400	y = −0.03ln(x) + 0.4696	0.9907	0.3314
12	38°13′52.7815″	118°51′30.6558″	50	5	162 782 1665	0.3430 0.4130 0.4350	y = 0.0402ln(x) + 0.1399	0.9915	0.3250
13	38°12′58.4168″	118°48′44.4721″	120	12	2 10 200	0.2780 0.2310 0.0750	y = −0.045ln(x) + 0.3193	0.9835	0.1121
14	38°15′56.3888″	118°49′06.2177″	40	4	19 102 598 2589 8372	0.7793 0.7142 0.5692 0.4523 0.4265	y = −0.063ln(x) + 0.9792	0.9774	0.6891
15	38°16′15.7953″	118°49′03.2053″	70	7	23 165 1042 2997 9471	0.8483 0.6870 0.5178 0.4892 0.4597	y = −0.067ln(x) + 1.0366	0.9555	0.7281
16	37°55′06.6434″	119°08′13.1352″	90	9	15 16 94	0.3154 0.3002 0.2338	y = −0.042ln(x) + 0.4222	0.9794	0.2288
17	38°13′52.9560″	118°47′27.7619″	20	2	3 17 77 306	0.2896 0.2473 0.2193 0.2086	y = −0.018ln(x) + 0.3033	0.9569	0.2204

Table A4. *Cont.*

No.	Longitude (E)	Latitude (N)	Lateral Consolidation Pressures (kPa) (σ3′)	Sampling Depth	Cycle Number	Dynamic Stress Ratio	Fitting Formula	R^2	CRR
18	38°11′49.3949″	118°48′04.5013″	20	2	339 1495 7508	0.4025 0.1801 0.1199	y = −0.09ln(x) + 0.8989	0.8863	0.4844
19	38°12′53.9775″	118°48′46.3513″	30	3	3 14 60 274	0.3712 0.2775 0.2080 0.1757	y = −0.044ln(x) + 0.4047	0.9585	0.2021
20	38°11′37.5267″	118°55′36.1643″	63	6.3	8 35 95	0.5097 0.4208 0.3537	y = −0.063ln(x) + 0.6429	0.9994	0.3528
21	38°13′40.2232″	118°56′58.1280″	140	14	7 47 90	0.3976 0.3406 0.3066	y = −0.035ln(x) + 0.4694	0.985	0.3082
22	38°16′03.9100″	118°50′42.5115″	50	5	232 254 2143	0.3100 0.2991 0.2400	y = −0.03ln(x) + 0.4681	0.9882	0.3299
23	38°14′36.9329″	118°47′24.9800″	50	5	10 25 63	0.7246 0.6138 0.5531	y = −0.095ln(x) + 0.9389	0.968	0.5014
24	38°13′40.2232″	118°56′58.1280″	100	10	11 31 64	0.3870 0.3580 0.3200	y = −0.036ln(x) + 0.4761	0.9574	0.3103
25	38°16′03.9100″	118°50′42.5115″	36	3.6	3 14 62 279	0.4780 0.3880 0.3140 0.2810	y = −0.044ln(x) + 0.5146	0.9653	0.3120
26	37°54′37.9495″	119°06′41.0577″	40	4	7 13 31	0.5528 0.4710 0.3300	y = −0.145ln(x) + 0.8346	0.9907	0.1669

Table A4. *Cont.*

No.	Longitude (E)	Latitude (N)	Lateral Consolidation Pressures (kPa) (σ3′)	Sampling Depth	Cycle Number	Dynamic Stress Ratio	Fitting Formula	R^2	CRR
27	38°08′35.3239″	118°53′55.8153″	80	8	4 15 65 262	0.3012 0.2079 0.1674 0.1451	y = −0.036ln(x) + 0.3297	0.9009	0.1639
28	38°08′58.7269″	118°54′31.0652″	100	10	4 16 66 274	0.3000 0.2267 0.1930 0.1740	y = −0.029ln(x) + 0.3219	0.9225	0.1884
29	38°19′12.0000″	118°59′24.0000″	50	5	1 5 123	0.4007 0.3008 0.2504	y = −0.029ln(x) + 0.379	0.8479	0.2455

References

1. Rahman, M.S.; Jaber, W.Y. A Simplified Drained Analysis for Wave-Induced Liquefaction in Ocean Floor Sands. *Soils Found.* **1986**, *26*, 57–68. [CrossRef] [PubMed]
2. Guo, X.; Fan, N.; Liu, Y.; Wang, Z.; Xie, X.; Jia, Y. Deep seabed mining: Frontiers in engineering geology and environment. *Int. J. Coal. Sci. Technol.* **2023**, *10*, 23. [CrossRef]
3. Wang, H.; Liu, H. Evaluation of storm wave-induced silt seabed instability and geo-hazards: A case study in the Yellow River delta. *Appl. Ocean Res.* **2016**, *58*, 135–145. [CrossRef]
4. Guo, X.; Fan, N.; Zheng, D.; Fu, C.; Wu, H.; Zhang, Y.; Song, X.; Nian, T. Predicting impact forces on pipelines from deep-sea fluidized slides: A comprehensive review of key factors. *Int. J. Min. Sci. Technol.* **2024**, *34*, 211–225. [CrossRef]
5. Guo, X.; Liu, X.; Zheng, T.; Zhang, H.; Lu, Y.; Li, T. A mass transfer-based LES modelling methodology for analyzing the movement of submarine sediment flows with extensive shear behavior. *Coast. Eng.* **2024**, *191*, 104531. [CrossRef]
6. Di Fiore, V.; Punzo, M.; Cavuoto, G.; Galli, P.; Mazzola, S.; Pelosi, N.; Tarallo, D. Geophysical approach to study the potential ocean wave-induced liquefaction: An example at Magoodhoo Island (Faafu Atoll, Maldives, Indian Ocean). *Mar. Geophys. Res.* **2020**, *41*, 9. [CrossRef]
7. Chávez, V.; Mendoza, E.; Silva, R.; Meneses, A.; Pérez, D.; Clavero, M.; Benedicto, I.; Losada, M. Failure of seabeds with a high mud content: An experimental study. *Coast. Eng. Proc.* **2014**, *1*, sediment.47. [CrossRef]
8. Damgaard, J.; Sumer, B.; Teh, T.; Palmer, A.; Foray, P.; Osorio, D. Guidelines for Pipeline On-Bottom Stability on Liquefied Noncohesive Seabeds. *J. Waterw. Port Coast. Ocean Eng.* **2006**, *132*, 300–309. [CrossRef]
9. Pilz, J.; Spock, G. Why do we need and how should we implement Bayesian kriging methods. *Stoch. Environ. Res. Risk Assess.* **2008**, *22*, 621–632. [CrossRef]
10. Fabijanczyk, P.; Zawadzki, J.; Magiera, T. Magnetometric assessment of soil contamination in problematic area using empirical Bayesian and indicator kriging: A case study in Upper Silesia, Poland. *Geoderma* **2017**, *308*, 69–77. [CrossRef]
11. Wang, Z.; Zheng, D.; Guo, X.; Gu, Z.; Shen, Y.; Nian, T. Investigation of offshore landslides impact on bucket foundations using a coupled SPH–FEM method. *Geoenviron. Disasters* **2024**, *11*, 2. [CrossRef]
12. Goeldner-Gianella, L.; Grancher, D.; Robertsen, Ø.; Anselme, B.; Brunstein, D.; Lavigne, F. Perception of the risk of tsunami in a context of high-level risk assessment and management: The case of the fjord Lyngen in Norway. *Geoenviron. Disasters* **2017**, *4*, 7. [CrossRef]
13. Du, X.; Sun, Y.; Song, Y.; Xiu, Z. Wave-induced liquefaction hazard assessment and liquefaction depth distribution: A case study in the Yellow River Estuary, China. *IOP Conf. Ser. Earth Environ. Sci.* **2020**, *569*, 012011. [CrossRef]
14. Fell, R.; Corominas, J.; Bonnard, C.; Cascini, L.; Leroi, E.; Savage, W.Z. Guidelines for landslide susceptibility, hazard and risk zoning for land use planning. *Eng. Geol.* **2008**, *102*, 85–98. [CrossRef]
15. Kvalstad, T.J. What is the Current "Best Practice" in Offshore Geohazard Investigations? A State-of-the-Art Review. In Proceedings of the Offshore Technology Conference, Houston, TX, USA, 30 April–3 May 2007. [CrossRef]
16. Liu, X.; Wang, Y.; Zhang, H.; Guo, X. Susceptibility of typical marine geological disasters: An overview. *Geoenviron. Disasters* **2023**, *10*, 10. [CrossRef]
17. Zhang, X.; Lei, L.; Xu, C. Large-scale landslide inventory and their mobility in Lvliang City, Shanxi Province, China. *Nat. Hazards Res.* **2022**, *2*, 111–120. [CrossRef]
18. Gamboa, D.; Omira, R.; Terrinha, P. A database of submarine landslides offshore West and Southwest Iberia. *Sci. Data* **2021**, *8*, 185. [CrossRef] [PubMed]
19. Locat, J.; Lee, H.J. Submarine landslides: Advances and challenges. *Can. Geotech. J.* **2011**, *39*, 193–212. [CrossRef]
20. Chang, C.; Chien, L.; Chang, Y. 3-D liquefaction potential analysis of seabed at nearshore area. *J. Mar. Sci. Technol.* **2004**, *12*, 2. [CrossRef]
21. Ishihara, K.; Yamazaki, A. Analysis of wave-induced liquefaction in seabed deposits of sand. *Soils Found.* **1984**, *24*, 85–100. [CrossRef]
22. Seed, H.B.; Idriss, I.M. Simplified Procedure for Evaluating Soil Liquefaction Potential. *J. Soil Mech. Found. Div.* **1971**, *97*, 1249–1273. [CrossRef]
23. Nataraja, M.S.; Gill, H.S. Ocean wave-induced liquefaction analysis. *J. Geotech. Eng.* **1983**, *109*, 17881. [CrossRef]
24. Youd, T.L.; Idriss, I.M.; Andrus, R.D.; Arango, I.; Castro, G.; Christian, J.T.; Dobry, R.; Finn, W.D.L.; Harder, L.F.; Hynes, M.E.; et al. Liquefaction resistance of soils: Summary report from the 1996 NCEER and 1998 NCEER/NSF workshops on evaluation of liquefaction resistance of soils. *J. Geotech. Geoenviron. Eng.* **2001**, *127*, 817–833. [CrossRef]
25. Vongchavalitkul, S. Probabilistic Safety Factor of Soil Liquefaction. *Appl. Mech. Mater.* **2012**, *217*, 2414–2418. [CrossRef]
26. Elishakoff, I. Interrelation between Safety Factors and Reliability. NASA/CR—2001-211309. 2001. Available online: https://ntrs.nasa.gov/api/citations/20020011027/downloads/20020011027.pdf (accessed on 1 November 2001).
27. Espósito, T.; Assis, A.; Giovannini, M. Influence of the Variability of Geotechnical Parameters on the Liquefaction Potential of Tailing Dams. *Int. J. Surf. Min. Reclam. Environ.* **2002**, *16*, 304–313. [CrossRef]
28. Madsen, O.S. Wave-induced pore pressures and effective stresses in a porous bed. *Geotechnique* **1978**, *28*, 377–393. [CrossRef]
29. Demars, K.R. Transient Stresses Induced in Sandbed by Wave Loading. *J. Geotech. Eng.* **1983**, *109*, 591–602. [CrossRef]
30. Zen, K.; Yamazaki, H. Mechanism of Wave-Induced Liquefaction and Densification in Seabed. *Soils Found.* **1990**, *30*, 90–104. [CrossRef] [PubMed]

31. Seed, H.B.; Rahman, M.S. Wave-induced pore pressure in relation to ocean floor stability of cohesionless soils. *Mar. Georesour. Geotechnol.* **1978**, *3*, 123–150. [CrossRef]
32. Horikawa, K. *Coastal Engineering: An Introduction to Ocean Engineering*; University of Tokyo Press: Tokyo, Japan, 1978.
33. Ameratunga, J.; Sivakugan, N.; Das, B.M. Standard Penetration Test. In *Correlations of Soil and Rock Properties in Geotechnical Engineering*; Ameratunga, J., Sivakugan, N., Eds.; Springer: New Delhi, India, 2016; pp. 87–113.
34. Bolton Seed, H.; Tokimatsu, K.; Harder, L.F.; Chung, R.M. Influence of SPT Procedures in Soil Liquefaction Resistance Evaluations. *J. Geotech. Eng.* **1985**, *111*, 1425–1445. [CrossRef]
35. Olsen, R. Normalization and Prediction of Geotechnical Properties Using the Cone Penetrometer Test (CPT). 1994. 326p. Available online: https://apps.dtic.mil/sti/citations/ADA285193 (accessed on 1 August 1994).
36. Tokimatsu, K.; Uchida, A. Correlation Between Liquefaction Resistance and Shear Wave Velocity. *Soils Found.* **1990**, *30*, 33–42. [CrossRef] [PubMed]
37. Kayen, R.; Moss, R.; Thompson, E.; Seed, R.; Cetin, K.; Kiureghian, A.; Tanaka, Y.; Tokimatsu, K. Shear-Wave Velocity–Based Probabilistic and Deterministic Assessment of Seismic Soil Liquefaction Potential. *J. Geotech. Geoenviron. Eng.* **2013**, *139*, 407–419. [CrossRef]
38. Cetin, K.O.; Seed, R.B.; Kayen, R.E.; Moss, R.E.S.; Bilge, H.T.; Ilgac, M.; Chowdhury, K. SPT-based probabilistic and deterministic assessment of seismic soil liquefaction triggering hazard. *Soil Dyn. Earthq. Eng.* **2018**, *115*, 698–709. [CrossRef]
39. Moss, R.E.S.; Seed, R.B.; Kayen, R.E.; Stewart, J.P.; Kiureghian, A.D.; Cetin, K.O. CPT-Based Probabilistic and Deterministic Assessment of In Situ Seismic Soil Liquefaction Potential. *J. Geotech. Geoenviron. Eng.* **2006**, *132*, 1032–1051. [CrossRef]
40. Lee, H.J. The Role of Laboratory Testing in the Determination of Deep-Sea Sediment Engineering Properties. In *Deep-Sea Sediments*; Springer: Boston, MA, USA, 1974; pp. 111–127. [CrossRef]
41. Iwasaki, T.; Arakawa, T.; Tokida, K. Simplified procedures for assessing soil liquefaction during earthquakes. *Int. J. Soil Dyn. Earthq. Eng.* **1984**, *3*, 49–58. [CrossRef]
42. Silva, M.P.N.; Guedes, C.C.; Vander, F.M.; Mascarenhas, R.D.O.; Salvador, F.A. Evaluating geostatistical methods along with semi-destructive analysis for forensic provenancing organic-rich soils in humid subtropical climate. *Forensic Sci. Int.* **2022**, *341*, 111508. [CrossRef] [PubMed]
43. Gribov, A.; Krivoruchko, K. Empirical Bayesian kriging implementation and usage. *Sci. Total Environ.* **2020**, *722*, 137290. [CrossRef] [PubMed]
44. Krivoruchko, K.; Gribov, A. Evaluation of empirical Bayesian kriging. *Spat. Stat.* **2019**, *32*, 100368. [CrossRef]
45. Jia, Y.; Zhang, L.; Zheng, J.; Liu, X.; Jeng, D.; Shan, H. Effects of wave-induced seabed liquefaction on sediment re-suspension in the Yellow River Delta. *Ocean Eng.* **2014**, *89*, 146–156. [CrossRef]
46. Liu, X.; Zhang, H.; Zheng, J.; Guo, L.; Jia, Y.; Bian, C.; Li, M.; Ma, L.; Zhang, S. Critical role of wave–seabed interactions in the extensive erosion of Yellow River estuarine sediments. *Mar. Geol.* **2020**, *426*, 106208. [CrossRef]
47. Zhang, H.; Lu, Y.; Liu, X.; Li, X.; Wang, Z.; Ji, C.; Zhang, C.; Wang, Z.; Jing, S.; Jia, Y. Morphology and origin of liquefaction-related sediment failures on the Yellow River subaqueous delta. *Mar. Pet. Geol.* **2023**, *153*, 106262. [CrossRef]
48. Chang, F. Study on Mechanism of Wave-Induced Submarine landslide at the Yellow River Estuary. Ph.D. Thesis, Ocean University of China, Qingdao, China, 2009.
49. Ma, B. Liquefaction of Seabed Silt under Storm Waves. Master's Thesis, First Institute of Oceanography, MNR, Qingdao, China, 2015. (In Chinese)
50. Wang, Z.; Du, X.; Sun, Y.; Song, Y.; Dong, L.; Zhou, Q.; Jiang, W. Risk zonation of submarine geological hazards in the Chengdao area of the Yellow River subaqueous delta. *Front. Mar. Sci.* **2023**, *10*, 1285437. [CrossRef]
51. Liu, X.; Lu, Y.; Yu, H.; Ma, L.; Li, X.; Li, W.; Zhang, H.; Bian, C. In-situ observation of storm-induced wave-supported fluid mud occurrence in the subaqueous Yellow River delta. *J. Geophys. Res. Oceans.* **2022**, *127*, e2021JC018190. [CrossRef]
52. Liu, Z.; Chen, Q.; Zheng, C.; Han, Z.; Cai, B.; Liu, Y. Oil spill modeling of Chengdao oilfield in the Chinese Bohai Sea. *Ocean Eng.* **2022**, *255*, 111422. [CrossRef]
53. Guo, X.; Liu, X.; Li, M.; Lu, Y. Lateral force on buried pipelines caused by seabed slides using a CFD method with a shear interface weakening model. *Ocean Eng.* **2023**, *280*, 114663. [CrossRef]
54. Chu, Z.X.; Sun, X.G.; Zhai, S.K.; Xu, K.H. Changing pattern of accretion/erosion of the modern Yellow River (Huanghe) subaerial delta, China: Based on remote sensing images. *Mar. Geol.* **2006**, *227*, 13–30. [CrossRef]
55. Zhang, H.; Liu, X.; Jia, Y.; Du, Q.; Sun, Y.; Yin, P.; Shan, H. Rapid consolidation characteristics of Yellow River-derived sediment: Geotechnical characterization and its implications for the deltaic geomorphic evolution. *Eng. Geol.* **2020**, *270*, 105578. [CrossRef]
56. Cao, L.H.; Zhai, K.; Pu, J.J.; Hou, Z.M.; Gao, W. Study on regional distribution pattern of subaqueous shore slope sediment movement in Chengdao sea area. *Geol. Environ. Sci.* **2013**, *29*, 49–54. (In Chinese)
57. Zhang, W.; Liang, R.; Mou, X. Sea Bottom Sediment Characteristics and Engineering Geologic Properties in the Chengdao Oil Field Sea Area. *Adv. Mar. Sci.* **2005**, *3*, 305–312. (In Chinese)